Dynamics of Coalescence in Hyperquenched Glassy Water Probed by X-rays

Johannes Giebelmann[1] (0000-0003-4529-5124), Tobias Eklund[2,3,4] (0000-0002-5851-3939), Christina M. Tonauer[1,5] (0000-0001-6859-5344), Lilli-Ruth Fidler[1] (0009-0008-6608-3845), Louisa E. Kraft[2,3] (0009-0000-7650-7498), Isabell Zick[2,3] (0009-0009-9241-6049), Niels C. Giesselmann[2,3] (0009-0002-8139-4357), Fiona Berner[2,3] (0000-0002-8285-2359), Leah Schwerdtfeger[2,3] , Randeer Gautam[5,6] (0000-0002-5887-526X), Robert P.C. Bauer[5,7] (0000-0002-2932-6683), Alexander Gierke[4,5] (0009-0007-1625-6309), Fabian Westermeier[5] (0000-0003-0696-206X), Felix Lehmkühler[5,8] (0000-0003-1289-995X), Katrin Amann-Winkel[2,3] (0000-0002-7319-7807), and Thomas Loerting[1,*] (0000-0001-6694-3843)

[1]Institute of Physical Chemistry, University of Innsbruck, Innrain 52c, 6020 Innsbruck, Austria
[2]Institute of Physics, Johannes Gutenberg University Mainz, Staudingerweg 7, 55128 Mainz, Germany
[3]Max Planck Institute for Polymer Research, Ackermannweg 10, 55128 Mainz, Germany
[4]European XFEL, Holzkoppel 4, 22869 Schenefeld, Germany
[5]Deutsches Elektronen-Synchrotron DESY, Notkestraße 85, 22607 Hamburg, Germany
[6]Department of Physics, University of Siegen, Adolf-Reichwein-Straße 2a, 57076 Siegen, Germany
[7]Freiberg Center for Water Research, Winklerstraße 5, 09599 Freiberg, Germany

*Correspondence to thomas.loerting@uibk.ac.at

Abstract

Dynamics, morphology, and structure of glassy water are highly relevant for cryochemical techniques, in particular for cryo–electron microscopy (cryo-EM). Here, we study the structural dynamics of a deposit consisting of thousands of micrometer-sized glassy water droplets during and after droplet coalescence using X-ray photon correlation spectroscopy (XPCS) at the micro- and mesoscale. We cover the temperature range from 94 to 161 K, encompassing droplet coalescence, the glass transition, and crystallization to ice I. Our experimental protocol involves heating beyond the coalescence regime, followed by recooling and reheating beyond crystallization, which allows us to disentangle the dynamics of coalescence from those associated with the glass transition. During coalescence, we observe an irreversible ballistic process in the temperature range between 130 and 145 K, with characteristic velocities of approximately 0.1–0.2 Å s^{-1}. In addition, samples that are not annealed below 125 K exhibit a q-independent mode (q^0) at 130-145 K, which only appears while coalescence is progressing. We regard this to be a collective relaxation connected to a mobile surface layer at the droplet interfaces. After coalescence is complete, we observe significant diffusive dynamics. In particular, we find a sharp increase in diffusivity to approximately 2 $Å^2$ s^{-1} at around 148 K, indicating the onset of pronounced diffusive motion. From these results we conclude that droplet coalescence is primarily governed by ballistic, non-diffusive dynamics below ~136 K, whereas strongly heterogeneous diffusive dynamics emerge at higher temperatures. We associate the abrupt increase in diffusivity after coalescence with the bulk glass-to-liquid transition.

Introduction

Amorphous ice is believed to be the most abundant form of water in the universe [1] and plays a crucial role in astrochemical processes. These include the formation of comparably complex molecules, such as amino acids, even under the harsh conditions of the interstellar medium [2]. On Earth, water's

amorphous forms mainly exist in laboratories, where the research is driven both by fundamental interest in water's anomalous properties [3] and technological application. The latter involves the freeze-drying process in pharmaceutical [4] and food industry [5] as well as cryopreservation [6]. The prime example here is cryo-electron microscopy (cryo-EM) [7], which involves hyperquenched glassy water (HGW) [8] to protect biological specimens at 77 K, where cryo-images are recorded with low thermal noise. HGW is prepared by plunge-freezing of very thin layers of aqueous solutions in a non-boiling liquid [9] or by ultrarapid cooling of micrometer-sized liquid water droplets [10]. HGW is crucial because it enables the vitrification of aqueous samples, preventing the formation of crystalline ice that causes freeze-concentration and dehydration, causing damages to cells, e.g., by changes in osmotic pressure. Ice crystals also puncture membranes or damage tissue by squeezing. Amorphous water on the other hand preserves biological specimens in a near-native, hydrated state, allowing for high-resolution imaging without the artifacts caused by ice crystals or air-water interface effects, such as protein denaturation and preferred orientation [11,12].

In our work HGW is prepared by spraying an aerosol of micrometer-sized droplets onto a cooled copper substrate [13], achieving cooling rates of $\sim 10^7$ Ks^{-1}. Such rates are necessary as the critical cooling rate of water is $6.4 \cdot 10^6$ Ks^{-1} [14], meaning that cooling at lower rates leads to crystallization instead of vitrification. HGW shows a droplet morphology with droplet diameters of a few micrometers [13] after deposition at 77 K. However, little is known about how the morphology, structure and dynamics of HGW evolve with temperature and pressure. This is of particular importance in cryo-EM, where temperature jump and revitrification protocols are often employed to make use of the HGW amorphous matrix dynamics. This lets experimenters switch back and forth between a native liquid and a glassy environment and probe transient configurations of proteins [15–17].

Recently [18], we used *in situ* scanning electron mircroscopy (SEM), combined with small angle X-ray scattering (SAXS) at the European XFEL to probe changes in HGW droplet morphology upon heating. Upon heating, we observed droplet interfaces vanishing between 125 and 145 K directly in the SEM, accompanied by a reduction in specific surface area (as extracted from the SAXS data). Time-resolved *in situ* SEM measurements revealed flow on the micrometer scale at and above 145 K, which is terminated by crystallization at 155 K. That is, droplets are static below 125 K, but highly dynamic above 125 K, where droplet coalescence takes place. This is followed by a highly dynamic sample up to the point of crystallization at 155 K, where a static image is seen in the SEM again.

While we could observe droplet coalescence (*i.e.*, the merging of droplets) in these experiments, we were unable to extract dynamics information such as time constants, velocities or diffusivities. However, such information is vital to understanding the cause and mechanism of HGW droplet coalescence. Previously we argued [18] that coalescence is driven by the mobility of water molecules above the glass transition. More specifically the calorimetric glass transition of low-density water (a.k.a., water's first glass transition $T_{g,1}$) is observed at $T_{g,1} \approx 124$ K (at a heating rate of 0.17 K min^{-1} [19]) and $T_{g,1} \approx 137$ K (at 30 K min^{-1} [20]). Based on this, we suggested that the onset of diffusive liquid dynamics allows the coalescence to occur. However, despite decades of research, the question whether or not water's first glass transition is a true glass-to-liquid transition still lacks a clear answer. Many studies [21–24] find diffusive dynamics upon exceeding $T_{g,1}$ or other evidence that speak for the formation of a liquid [25–28]. The definition of a liquid state entails a viscosity of less than 10^{12} Pa·s which, to the best of our knowledge, has never been measured directly. Thus, clear evidence for a glass-to-liquid transition is still missing. In fact, several studies [29–33] opposing this view exist, suggesting non-diffusive dynamics and/or the lack of a glass-to-liquid transition (a much more detailed discussion is provided in the discussion section and in a comprehensive review [34]).

This means we are left with two possible options that might explain the loss of droplet interfaces: (i) A genuine glass-to-liquid transition, leading to a metastable, supercooled and diffusive liquid or (ii) non-diffusive dynamics that carries water molecules across the interfaces, where nano- to micrometers need

to be crossed. Scenario (ii) requires a higher surface mobility, caused by, *e.g.,* a surface glass transition, that allows the droplets to sinter while the bulk stays glassy. In this case, the coalescence process would complete without diffusion. However, it does not exclude a glass-to-liquid transition at higher temperatures.

In order to distinguish between these options, we here study the nanoscale dynamics of HGW at 125 K and above using X-ray photon correlation spectroscopy (XPCS) in the small-angle X-rays scattering (SAXS) geometry. To this end we directly deposited HGW onto support grids, as described recently [18], and loaded them into a cryostat that is fitted into the P10 Beamline at PETRA III (DESY, Hamburg, Germany). The samples were heated in a stepwise manner, covering a temperature range between 94 and 161 K, where droplet coalescence was observed earlier [18]. XPCS makes use of coherent X-ray radiation, producing a so-called speckle pattern in the detector image which encodes the current disordered structural configuration of the sample. Structural dynamics are probed by following the temporal evolution of this speckle pattern. With this technique, we find that droplet coalescence, occurring between 125 and 145 K, is mainly driven by a non-diffusive, ballistic process. After droplet coalescence, above 145 K, we find a diffusive process characterized by a diffusion constant of up to ~2 $Å^2s^{-1}$.

Methods

Hyperquenching

Glassy water droplets (HGW) were produced using the well-established hyperquenching technique, invented by Mayer [8] and optimized by Kohl *et al.* [13] The procedure is identical to our recent experiments [18] and closely follows the procedure described in ref. [13] which is why we will only give a brief description here. An aerosol of liquid water droplets with a mean diameter of ~3 µm was produced using an ultrasonic nebulizer (LKB Instruments, Model 108). The aerosol is then picked up by a carrier gas which is dry nitrogen (2 L/min flow) in our case. The aerosol is then transported through a hose that is cooled using an ice bath to lower the water vapor pressure and to remove larger, already coalesced droplets. The hose is connected to a vacuum chamber that is pumped by a 3-stage pumping system. A turbo-molecular pump (Leybold-Heraeus, Model Turbovac 360) with a multi stage roots pump (Pfeiffer Vacuum, Model ACP15) as a backing pump and a powerful cryo pump (Air Products, Model DE-208L) are used to achieve a pressure of ~10^{-2} mbar during the deposition and a base pressure of ~10^{-5} mbar. The cooled droplet aerosol enters the vacuum chamber through an orifice with a diameter of 300 µm. Upon passing the orifice, the droplets reach supersonic speeds and subsequently hit a liquid nitrogen-cooled OFHC copper substrate with a support grid mounted onto it using two screws. The support grids are commercially available 50 µm thick copper SEM finder grids (Gilder SEMF3) with square holes with a length of 1.16 mm. The copper substrate is mounted on a removable cold finger, and the temperature is measured using a Pt-100 sensor on the cold finger. The droplets hitting the copper substrate and support grid experience a cooling rate [13] of ~10^6 to 10^7 Ks^{-1} and vitrify rapidly upon contact, resulting in a ~95 % amorphous deposit (see SM section S2). After 7 min of deposition, the sample is recovered by venting the chamber with dry nitrogen and then quickly removing the cold finger with the sample still mounted. The cold finger is then immediately submerged into a bath of liquid nitrogen to prevent the sample from undergoing any temperature-induced changes. Finally, the support grid with the ~150-200 µm thick HGW deposit is removed from the copper substrate under liquid nitrogen.

X-ray Photon Correlation Spectroscopy (XPCS)

To study the temperature dependent structural dynamics of HGW, we used X-ray photon correlation spectroscopy (XPCS). Figure 1A shows a schematic of the setup used at the beamline P10 at PETRA III (DESY in Hamburg, Germany). In essence, it is a combined wide- (WAXS) and small-angle X-ray scattering (SAXS) setup using highly coherent X-rays with an energy of 8.8 keV, focused to a beam size of 7.9 x 17 $µm^2$ using Compound Refractive Lenses (CRLs). Silicon attenuators were used to prevent

X-ray induced sample changes and dynamics (refer to SM section S6.2 for more details). The WAXS signal was recorded using a Dectris Eiger 500 K detector, placed at a distance of ~15 cm from the sample and covering a momentum transfer q of 1.25-2.9 Å^{-1}. The SAXS signal was recorded using a Dectris Eiger X4M placed 5 m downstream of the sample covering a q-range of 0.0016 to 0.1 Å^{-1}. This q-range corresponds to a length scale of ~6-390 nm in real space.

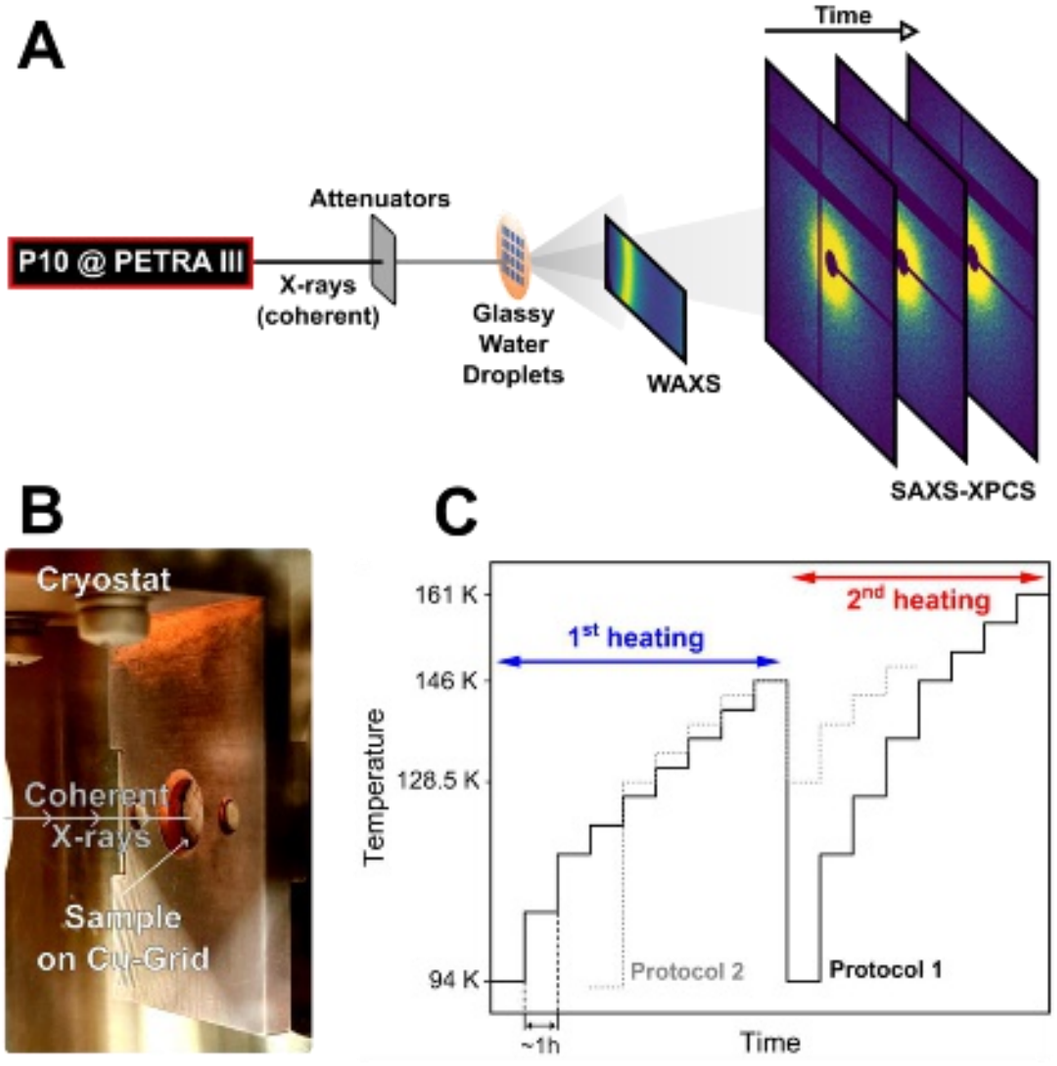

Figure 1: A: Schematic XPCS setup at the beamline P10 at PETRA III (DESY, Hamburg, Germany). Coherent X-rays are shot at the 150-200 µm thick HGW deposit mounted on a cryostat. Wide-angle scattering X-ray (WAXS) is used to observe the local structure (amporphicity/crystallinity) and XPCS measurements are performed in the small-angle scattering (SAXS) region. **B:** Picture of a sample grid mounted on the cryostat. **C**: Schematic representation of the temperature protocols used for this study. Heating between the isothermal steps was carried out at ~5 Kmin^{-1} while for cooling, the heating was simply switched off.

The WAXS signal holds information about the local atomistic structure of the sample, allowing us to monitor the amorphicity of our HGW samples and observe possible phase transitions, such as crystallization. The azimuthally integrated SAXS signal gives information regarding the morphology of the sample and lets us measure the specific surface area. As we have shown recently [18], this can be used to track droplet coalescence in HGW. Since we use coherent X-rays, the SAXS signal shows a speckle pattern that changes with time according to the structural dynamics present in the sample. For XPCS [35–38], we record a time series of the SAXS speckle patterns, allowing us to follow dynamics. The sample environment is a commercially available VPF-100 cryostat, manufactured by Janis Research Company. It is fitted with a custom-made copper sample holder that allows mounting of a 10 mm sample support grid as shown in figure 1B. The temperature is monitored using a DT-670 silicon diode on the

sample holder, connected to a Lake Shore temperature controller. Temperature control is achieved by heating elements connected to the controller and cooling using a steady flow of liquid nitrogen that is supplied by a transfer line. Each sample, sticking to its support grid, was loaded onto the pre-cooled cryostat submerged in liquid nitrogen. Subsequently, the cryostat was quickly placed into the sample vacuum chamber, which was then immediately pumped down to a pressure of ~10^{-4} mbar. The sample environment was directly connected to the beamline vacuum *via* vacuum shutters that were opened after pumping down. Typically, this setup has a temperature offset between the measured temperature and the actual temperature at the sample. This offset was calibrated by an internal calibration procedure, described in more detail in the SM, section S3. All temperatures in the main text were corrected for this offset.

The temperature protocols used for this study are shown schematically in figure 1C. The sample was heated in isothermal steps which lasted about an hour each. In the first 20 min, the sample was equilibrated in order to adjust to the new temperature and to eliminate any movement of the setup due to thermal expansion. Then, at least two consecutive 1000 s long XPCS measurements were performed while also recording the WAXS signal simultaneously. To improve statistics, the measurements were performed at two different spots on the sample each. When selecting a spot or measurement, we aimed for minimum crystallinity by monitoring the WAXS signal during spot change. Both protocols employ a first and a second heating run. The idea is that coalescence, as it is irreversible, should only occur during the first heating. In protocol 1, the sample spent a lot of time at low temperatures, as it was heated in steps starting from 94 K. Protocol 2, employed a temperature jump to 128.5 K, skipping these lower temperatures and thereby eliminating annealing effects.

Further, more in-depth information on the XPCS measurements, such as XPCS calibration using aerogel, assessment of beam-induced dynamics, as well as detailed sample information and preliminary characterization can be found in the SM.

XPCS, WAXS and SAXS Data Reduction

Per run, 1000 speckle patterns, each accumulated for 1 s, are recorded as 2D detector images with megapixel resolution. To extract dynamical information, this complex dataset is reduced to time correlation functions that capture the temporal evolution of the speckle pattern by correlating pixel intensities over time. This was done using the xpcsgui software package [39]. For this study, the time resolved speckle patterns were mainly reduced to the intensity autocorrelation function g_2 (equation 1) [35–38].

$$g_2(q,\tau) = \frac{\langle I(q,t)I(q,t+\tau)\rangle_{t,pix}}{\langle I(q,t)\rangle^2{}_{t,pix}} \quad (1)$$

Here, q is the momentum transfer given by $q = \frac{4\pi \sin\left(\frac{\theta}{2}\right)}{\lambda}$ for a certain scattering angle θ and wavelength λ, τ is the so-called lag time that passed since the initial time t, and I denotes the recorded pixel X-ray intensity. Averaging is first performed over t and then over pixels. Additionally, we calculated the two-time correlation function (TTCF) C as shown in equation 2 [35–38].

$$C(q,t_1,t_2) = \frac{\langle I(q,t_1)I(q,t_2)\rangle_{pix}}{\langle I(q,t_1)\rangle_{pix}\langle I(q,t_2)\rangle_{pix}} - 1 \quad (2)$$

Here t_1 and t_2 denote two different points in time for which the correlation map is calculated. In contrast to g_2, C is not averaged with respect to the initial time t. This means that C shows how much the dynamics change over time, *i.e.*, if the relaxation rate depends on the choice of t. Additionally, it can be used to quantify dynamical heterogeneities. To do so, we calculate χ which is the variance of C according to equation 3 and quantifies temporal heterogeneity of the measured dynamics [40].

$$\chi(q,\tau) = \langle C^2(q,t,t+\tau)\rangle_t - \langle C(q,t,t+\tau)\rangle_t^2 \quad (3)$$

The WAXS data were reduced by azimuthal integration using the pyFAI package for python [41]. Before doing so the pixel intensities were averaged over time. The SAXS data reduction was performed as part of the xpcsgui data reduction pipeline. That is, azimuthal integration and time averaging were carried out in a similar way to the WAXS data reduction.

Results

Static WAXS and SAXS Results

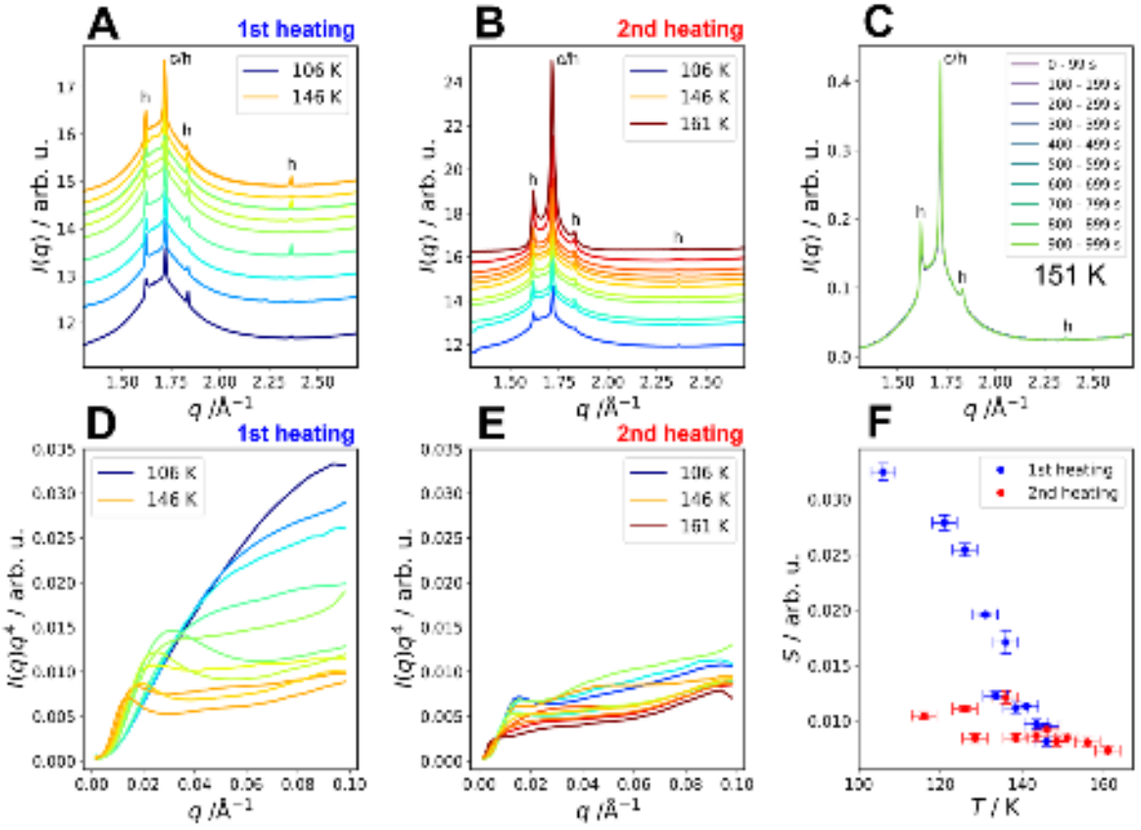

Figure 2: Results of time averaged scattering in the wide-angle (WAXS) and small-angle (SAXS) regime. All temperatures are corrected for an offset, see SM section S3 for details. **A/B:** Scattered intensity *I(q)* in the WAXS regime during the first (panel A) and second (panel B) heating cycle. The scattering profiles were normalized by the total scattered intensity and shifted with temperature for clarity. The letters h and c denote Bragg peaks of hexagonal and cubic ice I respectively. **C:** Time-resolved WAXS data during a measurement at 151 K. Please note ten curves are shown that are perfectly on top of each other, where each curve represents 100 seconds. **D/E:** Porod plots (see text) of the SAXS profiles for the first (panel D) and second (panel E) heating cycle, respectively. Before Porod scaling, *I(q)* was normalized using the invariant *Q* (see text). **F:** Surface parameter *S* determined from the Porod plots in panel D and E.

Figure 2A/B shows the WAXS scattering profiles (shown as intensity *I(q)*), normalized to the total scattered intensity in the available *q*-range and stacked by temperature. The pronounced halo peaks centered at 1.7 Å^{-1} confirm the HGW samples to be amorphous, more specifically to be low-density amorphous ice (LDA) [8]. Already at the start of the first heating cycle, minor contaminations of ice I (marked by the letters h and c in figure 2A) are found. These are typical for HGW where usually 95 % of the material is amorphous [13]. Based on calorimetry we estimate our HGW samples to be 91-94 % amorphous (see SM section S2 for details). Such contamination typically arises from condensation of water vapor onto the sample while loading and partial crystallization during hyperquenching. During the whole first heating cycle (up to 146 K), the dominating halo peak is conserved, meaning that the sample remains amorphous. Only small increases in the intensity of the Bragg reflexes of ice I are

observed, which might be a result of a spatially inhomogeneous distribution of the crystalline contaminants, as each measurement was performed at a different spot.

Also during the second heating cycle (figure 2B), the halo peak is conserved below ~156 K, showing that our samples stay amorphous below 156 K (blue to orange curves in figure 2B). Crystalline contamination is still observed during the second heating cycle and grows slightly when the temperature is increased, as the growing Bragg peaks show (yellow and orange curves in figure 2B). At 156 K, the samples crystallize partially (next to last red curve), and at 161 K (last red curve) the samples are fully crystalline. This is shown by the vanishing of the halo peak and simultaneous growth of the ice I Bragg peaks.

Since crystallization might interfere with our XPCS measurements, we investigate whether or not the WAXS signal changes with time during the measurement. This might pose a problem, especially at higher temperatures, where crystallization is faster. Figure 2C shows the WAXS signal at 151 K in a time-resolved manner. To this end the data are divided into chunks of 100 s each before reduction, showing how the local structure according to WAXS changes with time. Since all curves are practically identical in figure 2C, no progress of crystallization is observed on the timescale of our XPCS measurements. Neither the intensity of the halo peak decreases, nor the intensity of the Bragg reflexes increase. Thus, we conclude that below 156 K, crystallization does not progress on the time scale of our measurements and does not interfere with the XPCS analysis of the amorphous part of the sample. This is in line with earlier reports (see SI of ref. [23]).

Panel D and E of figure 2 show the normalized SAXS data for the first and second heating cycles, respectively. More precisely, in order to account for different thicknesses of the HGW sample at different spots the raw SAXS intensity $I_{\mathrm{raw}}(q)$ has been normalized using the invariant Q according to equation 4 [42],

$$I(q) = \frac{I_{\mathrm{raw}}(q)}{Q} = \frac{I_{\mathrm{raw}}(q)}{\int_0^\infty q'^2 I_{\mathrm{raw}}(q')\,\mathrm{d}q'} \tag{4}$$

where *I(q)* denotes the normalized SAXS intensity. The integration range is limited by the accessible q-range in SAXS, which means that Q can only be estimated. In other words, the normalization corrects for sample thickness, but some slight dependency on sample thickness still remains. Since *I(q)* is not known on an absolute scale, we cannot directly access the specific surface area from the SAXS scattering profiles. Instead, we define a surface parameter S in arbitrary units that is proportional to the specific surface area. According to Porod's law, the SAXS intensity in the high-q limit follows a Sq^{-4} decay [42]. To see if this behavior is followed, it is useful to rescale the data as $I(q)q^4$. This so-called Porod scaling has been done in figure 2D and 2E. All of the data there show a plateau in the high-q limit, in accordance with Porod's law. This part, in our case at least the q-range of 0.08-0.1 Å^{-1}, is caused by scattering from interfaces [42]. From the plateaus in figure 2D/E, we extract the surface parameter S as shown in equation 5.

$$S = \langle I(q)q^4 \rangle_{q\in[0.08\ \text{Å}^{-1},0.1\ \text{Å}^{-1}]} \tag{5}$$

Figure 2F shows the results for S based on the data in panels D and E. During the first heating cycle (blue points), the surface decreases strongly until ~145 K, but then remains constant upon further heating. During the second heating cycle (red points), S stays at a low value up to crystallization at 156 K, except for a few outliers below 140 K. This means that the sample's surface decreases irreversibly during the first heating cycle, with the strongest decrease occurring between 125 and 145 K. We reported the very same behavior recently based on XFEL measurements [18] and assigned it to the vanishing of droplet interfaces, *a.k.a.* coalescence (see short summary in the introduction). Since we find the same behavior here, this means that the HGW samples undergo coalescence between 125 and 145 K during the first heating cycle.

Dynamics Analysis: SAXS-XPCS Results

Two-time Correlation Function (TTCF)

We now want to discuss the structural dynamics in terms of our XPCS results to recover more information on droplet coalescence in HGW and dynamics of amorphous ice below and above the glass transition temperature T_g upon heating.

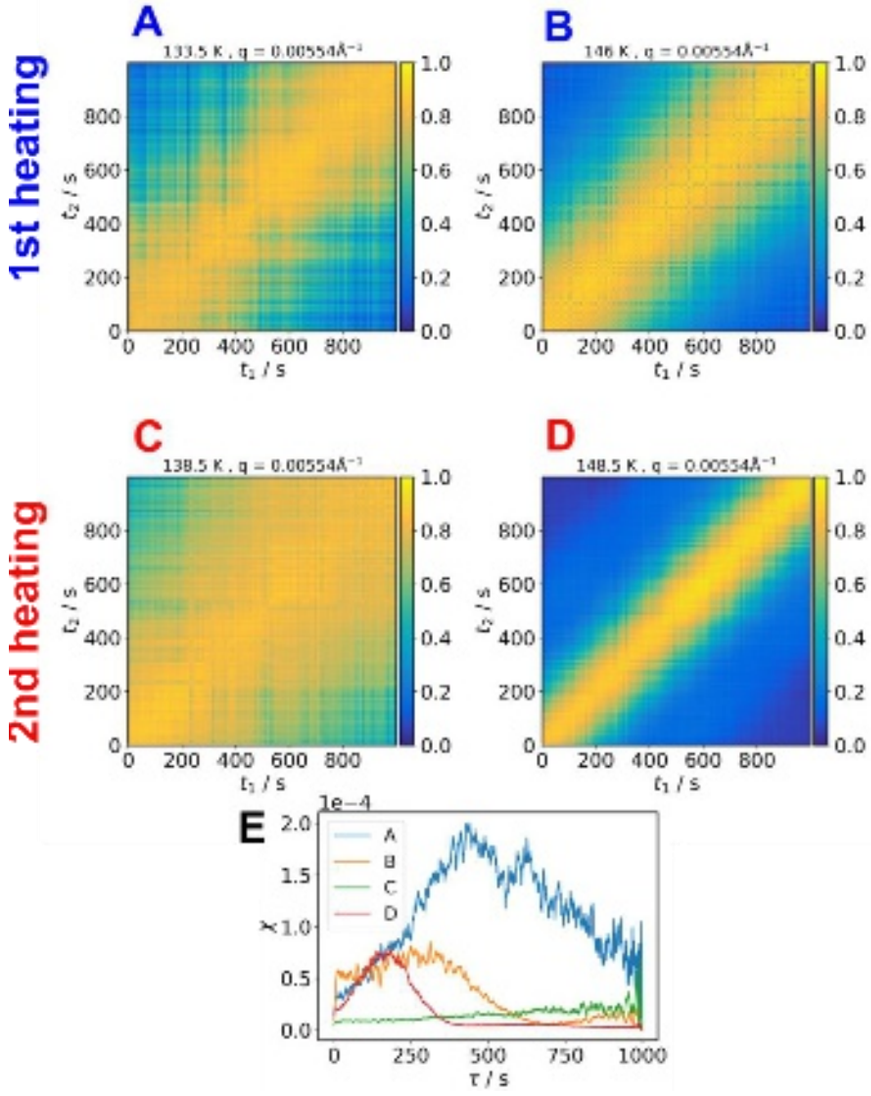

Figure 3: Exemplary normalized two-time correlation functions (TTCFs) at different temperatures calculated according to equation 2. The TTCFs have been corrected for systematic errors in baseline/contrast by rescaling. The data were selected as representative results for a low (133.5 and 138.5 K) and a high temperature (146 K and 148.5 K) during the first and second heating each. **A/B:** TTCF for two different temperatures during the first heating. **C/D:** TTCF for two different temperatures during second heating. **E**: Variance χ of the TTCFs shown in panels A-D calculated using equation 3.

Figure 3 shows some exemplary two-time correlation functions (TTCFs) for different temperatures during first and second heating. The TTCF and its normalized variance χ are useful tools to judge whether or not the observed dynamics correspond to equilibrium processes in the time frame of observation (in our case 1000 s) [43]. In case no strong fluctuations are visible in the TTCF, the dynamics can be considered equilibrated within the respective experimental time frame. Strong fluctuations along the diagonal on the other hand point to non-equilibrium dynamics. X captures temporal heterogeneities of the dynamics which are related to spatial dynamic heterogeneities [43].

For the first heating cycle (figure 3A/B), we observe some small fluctuations, visible as small line-like decorrelation events at both, 133.5 and 146 K, accompanied by an underlying, relatively stable slow decay. At 133.5 K (panel E) χ shows a broad peak centered at 400 s that spans the whole τ range. After increasing the temperature to 146 K (panel B), χ (panel E) decreases drastically, and its peak maximum shifts to ~300 s. Typically, the maximum of χ coincides with the characteristic relaxation time, meaning that this shift to shorter times indicates that structural relaxation is faster when increasing the temperature in the first heating cycle. Additionally, the pronounced reduction of χ with increasing temperature indicates that dynamical heterogeneity is reduced as well. For hyperquenched glasses, strong dynamical heterogeneity is expected as there are many spatially separated domains that each have their own relaxation time [44]. For HGW, the droplet structure adds onto this, possibly further creating spatial heterogeneities. This explains the broad peak of χ at the beginning of the first heating cycle (figure 3A). The reduction of dynamical heterogeneity upon heating shows that HGW undergoes pronounced thermal relaxation during droplet coalescence.

In the second heating cycle (figure 3C/D), the fast fluctuations observed during the first heating cycle vanish, indicating that they are caused by an irreversible, non-equilibrium process. Instead, the TTCFs of the second heating cycle show a stable main decay and significantly faster decorrelation at higher temperatures. The former indicates that we here observe equilibrated dynamics (on the timescale of 1000 s) while the latter indicates the speed-up of dynamics at higher temperatures. The low χ (figure 3E) in the second heating cycle further supports this. However, we note that χ has a peak at lag times of ~250 s after increasing the temperature to 148.5 K which is not found at 138.5 K. The reason for this might be the very slow dynamics of the sample at 138.5 K, shifting the peak of the variance outside of our observation range. Although dynamic heterogeneities are less during the second heating cycle, some are still observed. This is not surprising given that amorphous ice under these conditions is close to its glass transition temperature where dynamic heterogeneities are expected [43].

In essence, based on the TTCFs, we identify a fast non-equilibrium process along with pronounced dynamic heterogeneities during the first heating cycle. The second heating cycle by contrast features equilibrium dynamics on the time scale of the measurement. Given that this fast irreversible process coincides with the temperature range in which coalescence is observed (~125-145 K), it is likely coupled to or even caused by the coalescence process.

Intensity Autocorrelation Function (g_2)

Using equation 1, the observed speckle dynamics were reduced to the intensity autocorrelation function g_2. As seen in figure 4A, in some of the runs a fast initial decay within the first 10 s is observed in the first heating cycle. We note that this is mostly the case when using the heating protocol 2 (dashed line in figure 1C), which skips low temperature annealing by jumping directly from 94 to 128.5 K before continuing with step-wise heating. This fast initial decay is followed by a larger and much slower decorrelation. The fast mode is most intense at 143.5 K and less pronounced at lower and higher temperatures. Even more so, it is completely absent in the second heating cycle (figure 4B), where again a much slower decorrelation is observed that accelerates with temperature.

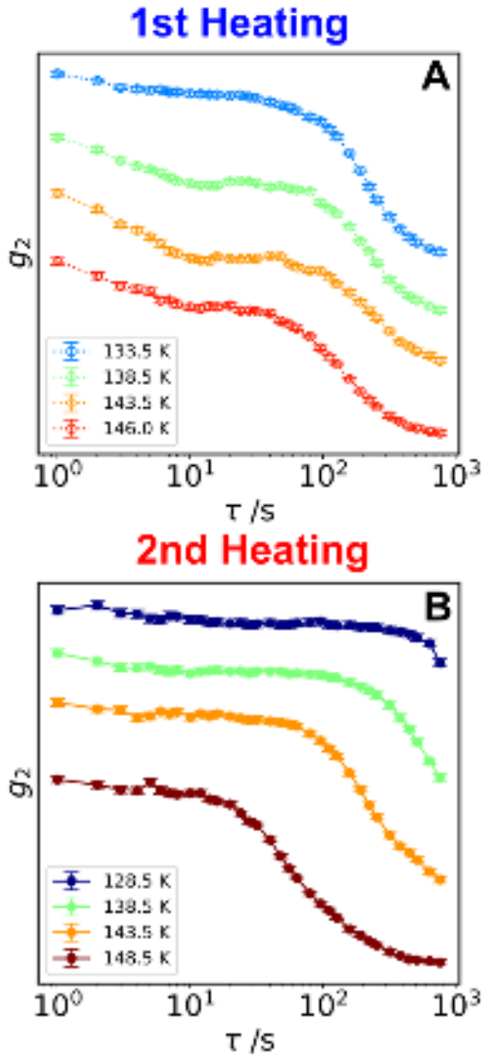

Figure 4: Raw intensity autocorrelation functions g_2 for protocol 2 (after rapid heating to 128.5 K). A vertical offset was applied for clarity. **A:** Exemplary g_2 functions for the first heating cycle. **B:** Exemplary g_2 functions for the second heating cycle.

When using protocol 1 involving long annealing of the sample below 130 K instead (see figure 1C and SM section S6.3), the fast initial decay within the first 10 s found in figure 4A is only present at 131 and 136 K, and it is much less pronounced. In fact, for most of the runs it is only the first data point that is slightly elevated, which is not enough to justify the existence of an additional fast decay. Also in the second heating cycle, the initial decay is not significant. This means, for protocol 1, the fast initial decay is only present around 131-136 K during the first heating after annealing the sample below 130 K.

That is to say, we observe an additional fast decay within the first 10 s of the measurement consistently when the sample is immediately heated to 128.5 K into the coalescence range of 125-145 K without prior annealing. Annealing the sample below 130 K causes this fast decay to fade away or even vanish fully in most runs. Clearly the dynamics observed during the first heating cycle are dependent on thermal history. This is rather expected, given the morphological changes during droplet coalescence and the decrease of specific surface area discussed earlier.

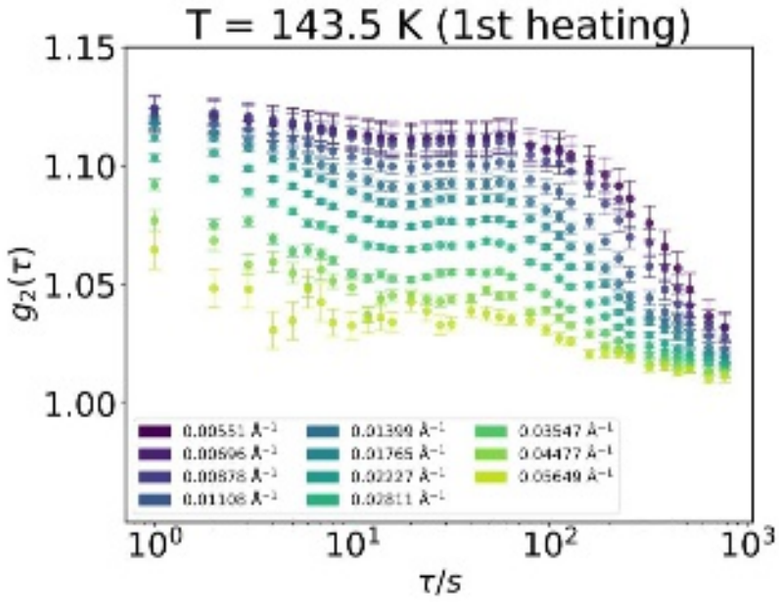

Figure 5: Raw intensity autocorrelation function g_2 for different q-values. The data were recorded during the first heating cycle using protocol 2, which includes the temperature jump to 128.5 K. Note that the initial fast decay ceases after ~11 s for all q bins, indicating that the relaxation rate is q-independent.

To clarify the type of process that the fast decay observed in figure 4A corresponds to, let us have a look at the raw g_2 functions in figure 5. For all q sections (or q bins), the initial decay ceases after ~11 s of lag time. This means that the relaxation rate is q-independent, although we do note that the decay appears stronger at higher q, meaning that the decrease of g_2 is larger. Fitting a model that adds a q-independent decay empirically shows that the relaxation rate is q-independent (see next section). Since other relaxational modes are usually associated with a q^n-dependence, where n is, *e.g.* 1 for ballistic processes and 2 for diffusion [35], we will refer to this q-independent mode as q^0 mode, implying $n = 0$.

But what is the origin of such a q^0 mode? Using molecular dynamics simulations of supercooled water and silica [45], it has been shown that a q^0 mode can originate from collective density-density correlations probed at larger length scales than the inter-particle distance, *i.e.*, at low q. This behavior is observed in many network-forming soft matter systems [45–47]. In this case a q^0 mode requires sufficiently large units that relax independently from each other, requiring all units to fully relax over all length scales to fully decorrelate [48]. This has been reported for vitrimers where the elastic modulus fluctuates locally with the same time scale at all length scales due to an underlying network bond swapping process [48]. Microscopically, HGW is a tetrahedral network of water molecules meaning that collective network dynamics could be at the origin of the q^0 mode. However, the q^0 mode is absent in all bulk amorphous ices studied previously by XPCS [23,24,49–51]. Our HGW samples differ from these bulk samples in that they feature internal surfaces, namely interfaces between droplets. The q^0 mode has to be linked to dynamics involving these internal interfaces across the sample. After coalescence the interfaces are missing, and also the q^0 mode is no longer present. Other possible causes of a q^0 mode were reported for polymer-based quasicrystals, which show q-independent relaxation linked to grain boundary dynamics [52]. This shows that interfacial effects can give rise to q-independent dynamics. We suggest the same to be the case for HGW, especially because a mobile surface layer was observed previously for amorphous ice in this temperature range [53]. This might enable collective motion across the droplet interfaces or even collective motion of the droplets as a whole, causing the q^0 mode. This explains why the q^0 mode is only observed during coalescence in the first heating run while the interfaces vanish. We do note that droplet coalescence is only one possible link to the q^0 mode, as such modes are a more general feature of soft-matter systems [45–47]. To fully resolve its origin, further experiments with different q-ranges are of interest. As evident in figure 5, the q^0 mode is less pronounced

at lower q, meaning that it might disappear when measuring at even lower q. At larger q this mode might either stay q-independent or develop a q-dependency. Knowing this q-dependency is key for investigating the origin of this relaxational mode.

Global Fitting Procedure

To extract dynamic information from g_2, a model description is necessary. A typical approach is to model g_2 empirically using a (stretched) exponential decay. However, here we expect several components, including diffusion and ballistic movement of water molecules. X-rays are mostly sensitive to the positions of the oxygen atoms, meaning that we resolve translational motion, but not H-atom jumps or molecular rotation. Given the q-range of our experiment (0.0016 to 0.1 Å^{-1}), we probe motion at the length scale of ~6-390 nm. Diffusion and ballistic movement on a similar length scale were reported earlier for other types of amorphous ice [23,24,49,50,54]. Modelling g_2 directly with a sum of (stretched) exponentials might in this case be inaccurate and limit the physical reliability of the parameters that are extracted from the fits. This is because such a direct description is purely empirical, without an underlying physical argument. Additionally, often the cross terms that inevitably arise when squaring F according to the Siegert relation [35] (equation 6) are neglected.

$$g_2(q,\tau) = b + \beta|F(q,\tau)|^2 \tag{6}$$

Here, b is the baseline of g_2 and β is the speckle contrast. For this reason, we follow the approach of directly modelling the intermediate scattering function F instead of g_2 as described previously [50,54]. Initially, assuming a diffusive process characterized by the diffusivity D and a ballistic process characterized by the velocity v we can write F as equation 7 [50].

$$F(q,\tau) = Ae^{-(vq\tau)^2} + (1-A)e^{-(Dq^2\tau)^\gamma} \tag{7}$$

A is a weighting parameter and γ is the stretching parameter. This means we allow the distribution of diffusivities to be broadened according to γ while assuming a very sharp distribution (technically a single value) for v [54–56]. Equation 7 is strictly speaking only valid for the self-part of F meaning that collective movement of particles or density fluctuations is not covered [35]. Using the Siegert relation (equation 6) g_2 evaluates to equation 8 [50].

$$g_2(q,\tau) = b(q) + \beta(q)\left(Ae^{-(vq\tau)^2} + (1-A)e^{-(Dq^2\tau)^\gamma}\right)^2 \tag{8}$$

Now equation 8 can be fitted as a "global" fit to our g_2 data as described previously [50]. The term global here denotes that g_2 is fitted in q and τ simultaneously [57], which in our case means that a surface is fitted to the $g_2(q,\tau)$ data.

Figure 6A shows an exemplary global fit of g_2 using equation 8 and the procedure described above. For a simpler representation, the fitted surface is shown as individual line segments at the corresponding q values. We note that the model fit overall agrees well with the measured data. Typically, global fits perform worse than fitting each q value separately since the whole dataset is now described with (in our case) only two relaxation rates, whereas individual fits would employ two relaxation rates per q value. On the other hand, to extract v and D from the individual fit requires a second step where the q dependence of relaxation rates is fitted, effectively reducing the number of parameters again. As reported previously, these fits tend to deviate more from the measured data [23,49] - which means that the deviation from the model is shifted to this second step. Additionally, when using a non-global fit, the relaxation rates often turn out unreliable for very low or high q values. In the former case, the signal to noise ratio is often quite good due to a higher contrast but the decay is slower and if it is cut off, then the resulting relaxation rate(s) might be unreliable. This is less of a problem at large q since the decays are usually faster but also the contrast is lower, worsening the signal to noise ratio. Since this is also the

case for our dataset, a global fit and hence the analysis shown in Figure 6A is more suitable, allowing it to extract reliable data from all q values.

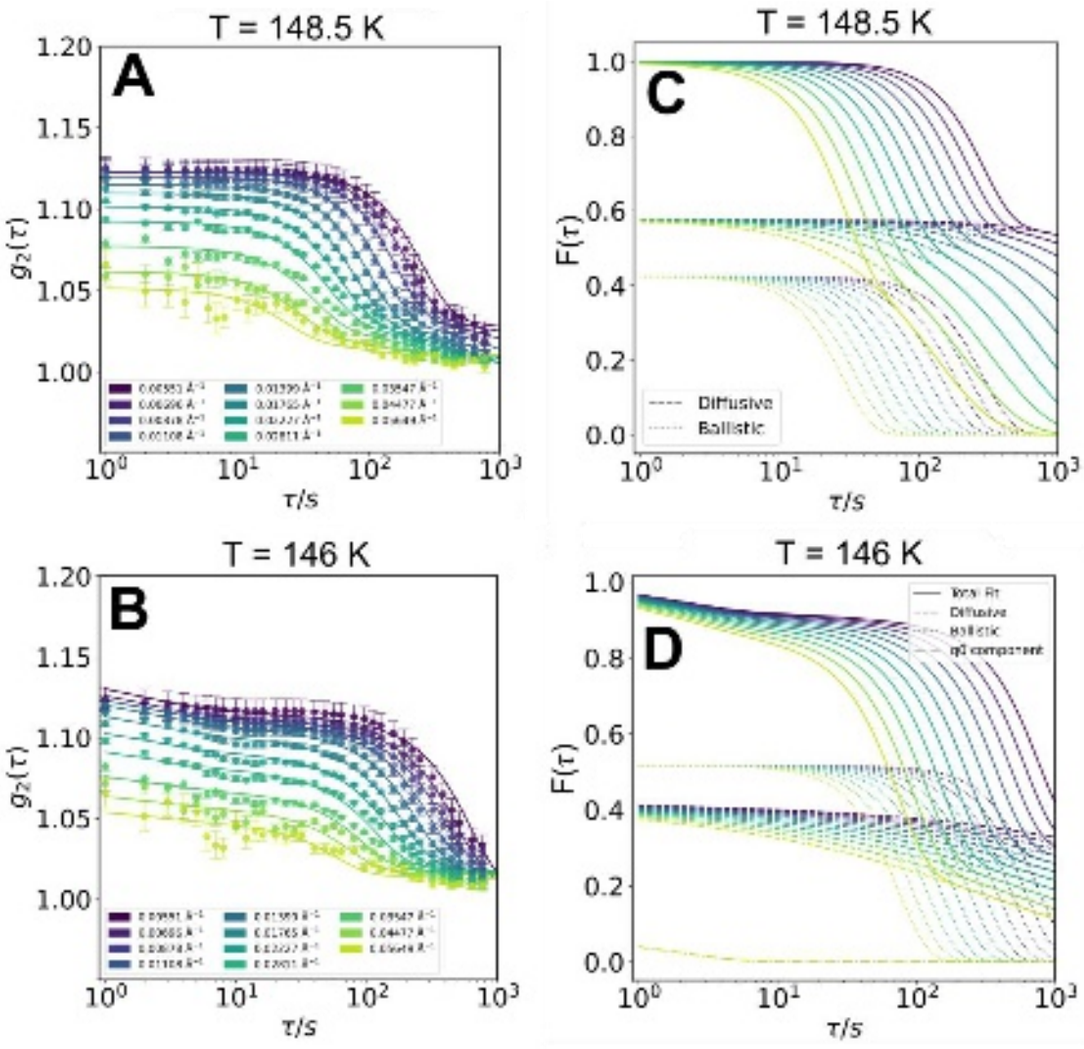

Figure 6: A: Exemplary fit to g_2 data that lacks a clear q^0 mode using equation 8. **B:** Exemplary fit to g_2 data that contains a clear q^0 mode using equation 9. Points represent measured data while solid lines indicate the global fit. In both cases a global surface fit procedure was applied (see text). **C/D:** Intermediate scattering function reconstructed from the corresponding fits, including decomposition into individual components.

Data that show a significant q^0 mode (see figure 5 and 6B), meaning that the decay is clearly visible over several data points, cannot be described by equation 8. To fix this, we introduce an exponential decay with a q independent relaxation rate Γ to F (equation 9).

$$g_2(q,\tau) = b(q) + \beta(q)\left(Ae^{-(\nu q\tau)^2} + Be^{-(Dq^2\tau)^\gamma} + (1-A-B)e^{-\Gamma\tau}\right)^2 \qquad (9)$$

Here A and B are weighing factors and for fitting, the sum of all three pre-exponential factors is constrained to 1. An exemplary global fit of equation 9 to experimental data is shown in figure 6B. Overall, the fit agrees well with our experimental data. In panels C/D of figure 6, the fits from panels A/B were plotted as separate curves per dynamical component. In all cases (no matter if q^0 is present or not) the main decay is explained by a ballistic component. The diffusive component is only significant at higher temperatures where it is visible as an additional shoulder at longer lag times, between 100 and 1000 s. The q^0 mode (if present) is always assigned to the initial fast decay.

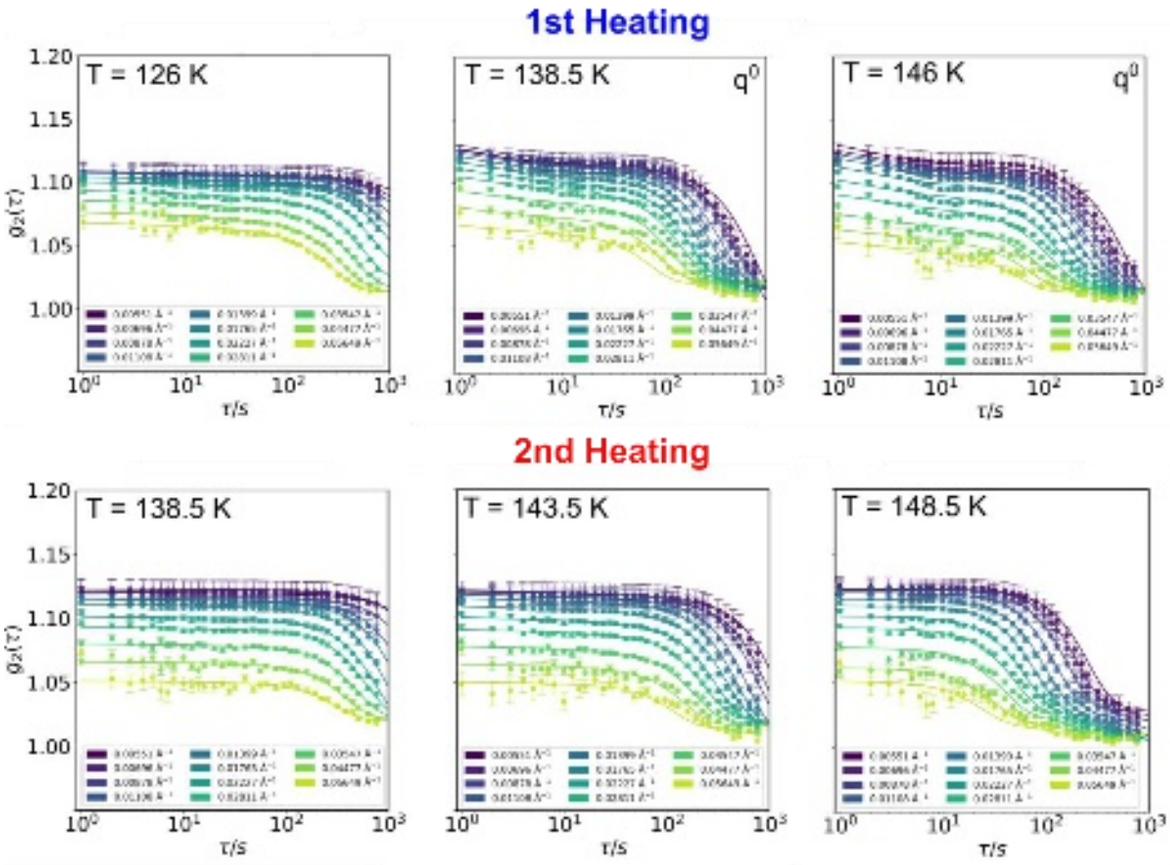

Figure 7: Exemplary g_2 data as a function of temperature during first and second heating including global surface fits of equation 8 or 9, respectively. All runs where a q^0 mode was unambiguously identified were fitted with equation 9 and are labelled accordingly. Runs that do not show this mode were fitted with equation 8. For the fits of the remaining data see SM section S6.3.

Figure 7 shows more exemplary fits of the previously described models to our experimental data. All data that unambiguously show the q^0 mode were fitted using a global fit of equation 9. The data that show no clear q^0 mode were fitted using equation 8. The remaining fits not shown in figure 7 are found in the SM section S6.3.

The fits using the q^0 model (middle and right panel in the upper row in figure 7, first heating) overall agree with the experimental data, although some deviations are noted. Mainly, the strength of the fast q^0 decay (within the first 10 s) is underestimated by the model. Additionally, the fits tend to overestimate the baseline at higher q values. This leads to a large error bar of the diffusivity since the diffusive decay is then not captured as well (see figure 8B). However, the main decay, which originates from the ballistic mode, is still captured reliably with a reasonable error bar (see figure 8A). Thus, we expect that at least v can be determined reliably from all of the q^0 model fits while D has a larger error. We also do note that the description improves substantially at higher temperatures. That said, the description of the q^0 mode could possibly be improved overall. Since the q^0 mode is likely caused by some kind of collective motion [45] this has to be considered when formulating F in an analytic fashion. However, this likely requires keeping the distinct part of the dynamic structure factor, which is usually omitted in the derivation. This, requires a detailed model of the underlying collective process.

When the q^0 mode is absent (lower row in figure 7, second heating), we find an excellent description using equation 8 for most runs. Deviations are usually limited to the higher q values which is expected due to the lower contrast and thereby lower signal to noise ratio.

Fit Results

The resulting parameters from the fits of equation 8 and 9 to all available g_2 data are shown in figure 8. Let us first discuss the ballistic velocity v shown in figure 8A. During the first heating cycle (blue symbols), we notice that from ~130 K on, v is significantly larger compared to the second heating (red symbols). For example, at 138 K we notice a difference of ~0.1 Ås^{-1} between the first (v ~ 0.15 Ås^{-1}) and the second heating cycles (v ~ 0.05 Ås^{-1}). Given a root mean square displacement $\mathrm{RMSD} = \sqrt{6}v\tau$ with a lag time of 1000 s, this results in an RMSD of ~370 Å for the first and an RMSD of ~120 Å for the second heating cycles. This means that the ballistic process either slows down after the first heating cycle or is of a different nature in the second one. Either way, the effect is at least partly irreversible. Even more so, this irreversible ballistic relaxation occurs in the temperature region where droplet coalescence occurs, namely between 125 to 145 K according to our recent study [18] and the SAXS data shown in figure 2. This suggests this irreversible ballistic mode during the first heating is caused or at least influenced by droplet coalescence. During the second heating, v stays below 0.1 Ås^{-1} until ~145 K, likely reflecting some slow ballistic glassy relaxation. This is quite common in glasses [58] and has been observed previously for other amorphous ices as well [23]. Upon exceeding 146 K during the second heating, v increases substantially, indicating significant ballistic relaxation.

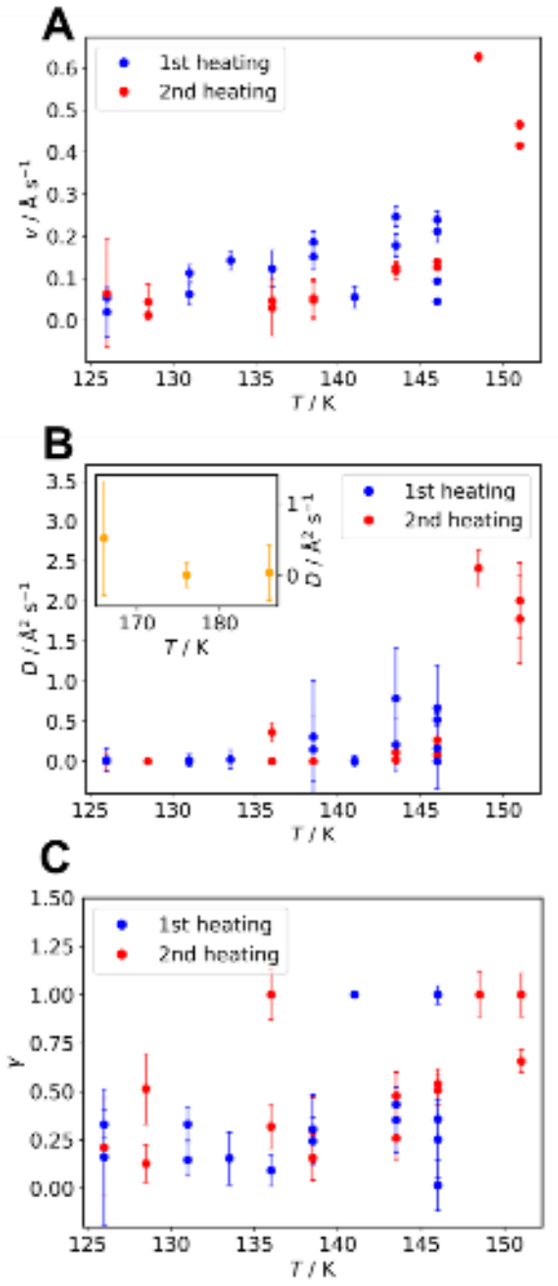

Figure 8: Parameters derived from the fits of equation 8 and 9 to the g_2 data. As discussed before, equation 9 is only used in case a clear q^0 mode is present. Blue symbols correspond to the first and red symbols to the second heating cycle each. For clarity, the temperature error bars of ±3 K are omitted. **A:** Velocity v of the ballistic process. **B:** Diffusivity D of the diffusive component. Inset: Diffusivity from data recorded after crystallization (see SM section S6.5 for details) **C:** Stretching exponent γ of the diffusive component.

Information on the diffusive relaxation is provided by the diffusivity D (figure 8B) and the stretching exponent γ (figure 8C). During the first heating cycle, D is quite close to zero for most of the runs, indicating very slow diffusion that is barely within our experimental time scale. A few runs however, especially around 145 K, show D values scattered around 0.5 $Å^2s^{-1}$ but with a large error bar. γ is quite low for almost all runs during the first heating, typically around 0.25. As γ can be interpreted as a width parameter of the underlying distribution of diffusivities [50,55], a low value corresponds to a broad distribution, whereas a value of 1 indicates a single diffusive process. That is, γ captures dynamical heterogeneities as a broad distribution of diffusivities [54]. The low values of γ during the first heating cycle indicate spatially heterogeneous dynamics during droplet coalescence. This combined with the

low diffusivity and fast ballistic relaxation suggests that the droplet coalescence is driven by a ballistic, non-diffusive relaxation instead of a bulk glass-to-liquid transition.

During the second heating, D stays close to zero up to 146 K, where a slight increase, followed by a huge jump to values of 2-2.5 $Å^2s^{-1}$ around 150 K is noted. This sudden increase of diffusivity is accompanied by γ jumping towards 1. This means from at least 146 K, we observe significant diffusive dynamics which speed up even more around 150 K and are accompanied by a reduction of dynamical heterogeneities. Since this occurs after the droplet coalescence has already reached completion, we infer a bulk amorphous ice that exhibits diffusive dynamics during the second heating.

The inset on figure 8B shows diffusivities measured *after* crystallization to stacking disordered ice I (see SM section S6.5 for details). As one can see, the diffusivity in ice I above 156 K is much lower than in amorphous ice around 150 K. This maximum of diffusivity, combined with the increased ballistic velocity at around 150 K indicates that non-crystalline water exhibits a state of comparably fast structural dynamics below its crystallization temperature.

Discussion and Conclusion

We have carried out two heating cycles on hyperquenched glassy water (HGW) composed of many micron-sized glassy droplets. In the first heating cycle the droplet interfaces disappear ultimately resulting in full coalescence. In terms of static properties the specific surface area, derived from the SAXS data, matches our earlier XFEL data [18] on irreversible droplet coalescence of micrometer-sized glassy water droplets in the temperature range between 125 and 145 K. In terms of dynamic properties our SAXS-XPCS measurements reveal an irreversible fast ballistic process and (depending on the thermal history) a very fast irreversible q^0 mode during the first heating cycle. Both the ballistic process and the q^0 mode are linked to the disappearance of droplet interfaces. At the same time the diffusivity is quite low in most cases with a low stretching exponent, indicating spatially heterogeneous dynamics. In the second heating cycle the sample no longer contains droplets, but represents a bulk amorphous ice, more specifically bulk low-density amorphous ice. In this second cycle a slower ballistic process typical of bulk glasses is observed below 146 K while the diffusivity stays low. When exceeding 146 K, the diffusivity and ballistic velocity increase rapidly. The diffusivity exhibits a maximum of ~2.5 $Å^2s^{-1}$ at around 150 K, just before crystallization, and the stretching exponent approaches 1. This indicates that the state above T_g contains less dynamic heterogeneities than the glass below T_g.

Dynamics of Droplet Coalescence (First Heating Cycle)

Using these findings, we can now clarify the root cause for the coalescence of HGW droplets between 125 and 145 K: In the introduction we discussed several scenarios regarding the dynamics that could drive the droplet coalescence. In essence, the question is if (i) a bulk liquid-to-glass transition gives the water molecules enough mobility to allow coalescence or (ii) if the coalescence is driven by non-diffusive, glassy dynamics. Since we find an irreversible ballistic process and a clearly non-diffusive q^0 mode during the first heating, scenario (ii) applies here. This is further backed up by the very slow and stretched diffusive component. If a bulk glass transition caused coalescence (scenario (i)) we would expect a substantial increase of the diffusivity below 125 K, where the coalescence starts. In other words, passing through the bulk glass transition is not required to induce droplet coalescence in HGW. The nature of the non-diffusive coalescence process, however, is difficult to extract from our data. Possibly it is a surface driven effect, meaning that the surface dynamics are faster than the bulk dynamics, allowing sintering of the droplets. A recent study using dielectric techniques reports the observation of such a mobile surface layer in amorphous solid water (ASW), even below 136 K [53]. More precisely, even at deposition temperatures below 80 K, a 1-3 nm thick mobile surface layer is present, which grows to 30 nm by deposition at 140 K. Depositing above 115 K, where the layer is ~10 nm thick, results in sintered ASW (a.k.a. compact ASW or c-ASW). This means already at 115 K, the surface dynamics are fast enough in ASW to allow pronounced morphology changes. We expect that such a mobile surface layer is also present in other types of amorphous ice, especially at the droplet surfaces of HGW. Thereby,

bridges between individual droplets may form *via* the mobile surface layer. These bridges then spread across the interfaces and connect the droplets. This might be the very process at the origin of the ballistic mode linked to coalescence. The dynamic surface layer then probably revitrifies after the transition from 2D material containing interfaces to interface-free bulk 3D material is complete. This explains why coalescence starts below T_g and does not need diffusive bulk dynamics if long-term annealing below T_g is done as in our protocol 1. If on the other hand the long-term annealing below T_g is skipped, as in our protocol 2, then coalescence takes place in a slightly different way. Then the collective dynamics also involve the bulk, the *q*-independent mode appears in addition to the ballistic mode, where both contribute to the coalescence.

Dynamics of Bulk Glassy Water (Second Heating Cycle)

After coalescence has reached completion, we do observe rather fast diffusion (D~2.5 $Å^2s^{-1}$) at around 150 K with the onset at ~145 K. For vapor deposited amorphous solid water (ASW) a diffusivity of 0.625 $Å^2s^{-1}$ was reported at 136 K as measured by isotope diffusion[22] and 1 $Å^2s^{-1}$ using XPCS [24]. Another study, tracking the pore collapse of ASW using small angle neutron scattering found a diffusivity of ~0.01 $Å^2s^{-1}$ between 120 and 136 K during the pore collapse[59]. These values agree in principle, considering that they are derived from different methods, length-scales, temperatures and samples of different morphologies.

The remaining key question is what causes the strong rise in diffusivity between 145 and 150 K during the second heating cycle in our experiments. For this, let us briefly discuss the literature on the dynamics of amorphous ice in this temperature regime (for a more detailed discussion see for example ref. [34]). Using calorimetry, the well-known heat capacity increase of HGW at 136 K (30 K/min heating rate) was observed [60] and assigned as a glass transition to supercooled liquid water (*a.k.a.* $T_{g,1}$), just before crystallization. Further support for this scenario is given by the finding that this heat capacity increase is a general feature of low-density type amorphous (LDA) ices [19,25,61]. Many more calorimetric studies employing different protocols, testing annealing effects [13,62], reversibility and isotope effect [20] of $T_{g,1}$, found that the observed heat capacity increase fulfills all calorimetric criteria of a glass-to-liquid transition. Volumetry, where the volume change under pressure as a function of temperature is recorded, reveals a sudden change of compressibility in a similar temperature range, indicating a softening of LDA, consistent with the glass-to-liquid scenario [63]. A similar result was obtained by a penetration study using a blunt indentor [26]. Isotope diffusion experiments [21,22] between layers of ASW labelled with different hydrogen or oxygen isotopes show layer intermixing and translational diffusion of water molecules. Dielectric spectroscopy [25–27] finds relaxation times compatible with a glass-to-liquid transition. A very recent study, combining dielectric spectroscopy and calorimetry data, concludes that $T_{g,1}$ at 136 K is indeed a α-relaxation glass transition [64]. Earlier XPCS studies reported diffusive dynamics of LDA after undergoing a polyamorphic transition [23] and at the glass transition temperature of ASW [24]. All these results are consistent with LDA-type amorphous ices, including HGW [65], undergoing a glass-to-liquid transition at 136 K where translational diffusion sets in. However, several studies report observations that are inconsistent with this scenario and instead suggest alternatives. These include the idea of a shadow glass transition, a well-known phenomenon for many hyperquenched glasses that represents an annealing effect and precedes the actual glass-to-liquid transition [44]. Based on the comparison with other hyperquenched systems, it was suggested that this is the case for water at 136 K [66] while the true glass-to-liquid transition would be located at 165 K, but preempted due to crystallization. This suggestion was later contested [26,27,62] after which more evidence for [33] and against [67] the shadow glass transition scenario was gathered. Another study using photochemical proton injection into ASW made from D_2O [29] suggested the onset of defect dynamics instead of a glass transition is the true nature of $T_{g,1}$ which again was contested later on [68]. The isotope effect (using $H_2{}^{18}O$ and D_2O) on the calorimetric glass transitions of LDA, HDA and ice VI was reported as essentially identical based on which a purely rotational glass transition was suggested [30]. This was interpreted as molecular rotations that set in above T_{g1}. Later it was shown that also

translational modes do not exhibit a significant $H_2{}^{18}O$ isotope effect, so that the absence of the isotope effect does not speak for the absence of translations [69]. Single molecule spectroscopy [70] studies on the other hand probed for the rotation of a marker molecule as a hallmark of the glass-to-liquid transition. In HGW, no rotation was observed suggesting that it stays solid above 136 K. This is in line with inelastic X-ray scattering measurements that show a crystal-like phononic band structure for amorphous ices [71,72]. Recently, also the possibility of a β-process being at the origin of $T_{g,1}$ was discussed [73]. Additionally, recent studies of confined water [32] revisit the possibility of a shadow glass transition as they find glass-to-liquid transitions between 170 and 200 K for their confined systems.

Although being just a brief summary, the previous paragraph shows nicely that water's glass transitions are far from being understood and are highly contested. Regarding $T_{g,1}$, likely only a viscosity measurement of LDA upon heating could solve the question whether or not a liquid forms. However, we do note that the repeated finding of diffusive dynamics around 136 K is a strong case for the glass-to-liquid transition scenario for bulk amorphous ice, including HGW after droplet coalescence. Additionally, most of the above-mentioned conflicting evidence heavily relies on the comparison with heavily confined water or even other glass-formers, which is interesting but cannot be used to unambiguously clarify the behavior of bulk water. Our finding of diffusive dynamics on the nanoscale before crystallization sets in, speaks for a glass-to-liquid transition after complete coalescence. As discussed above, the coalescence process itself is non-diffusive and occurs at lower temperatures than the diffusivity spike. We want to stress that this diffusion occurs after extensive annealing even above 136 K (due to the long measurement and equilibration times, the samples are automatically annealed, see figure 1C). This suggests that a shadow glass transition is rather unlikely. It is of course also inconsistent with all scenarios that exclude diffusivity at $T_{g,1}$, such as a purely rotational glass transition. Thus, based on our diffusivity data, along with several sophisticated experiments discussed in the previous paragraph, we suggest a glass-to-liquid transition as the most likely scenario at $T_{g,1}$ for bulk amorphous ice.

Another interesting finding is that in our case the diffusivity starts to increase at around 145 K, almost 10 K above the accepted literature values of $T_{g,1}$ [60]. The reason for this is likely that the dynamics probed in our SAXS experiments cover the microscale (~6-390 nm), whereas other measurements typically cover dynamics at the molecular distances (0.3-1.0 nm). Consequently, the dynamics probed by us over these large distances is slower than the molecular dynamics.

Lastly, we want to compare our results to previous XPCS investigations of other types of amorphous ice. Vapor-deposited amorphous solid water (ASW) [24] shows an even more complex relaxation behavior. Besides two major slow relaxational components, each composed of a diffusive and a ballistic one, additional fast components are reported. In terms of diffusivity, the slow component is very similar to the one we report here ($D \sim 1$ Å^2 s^{-1}) while the fast processes (~100 Å^2 s^{-1}) were linked to the collapse of micropores in ASW. After the morphology changes encountered in the first heating run, ASW and HGW feature similar dynamics in the second heating run. This reflects that both of them feature the dynamics of bulk LDA [65]. This also applies to LDA made via the polyamorphic transition from high-density amorphous ice (HDA). In this case fast diffusive dynamics were only observed during the transition and slow diffusion was observed afterwards [23,51]. Later, using thin free-standing HDA samples, a heterodyne signal observed in XPCS when approaching the polyamorphic transition to LDA [49]. It was shown that the heterodyne signal is due to diffusion of static LDA domains within the high-density matrix. This suggest the high-density part to be in a supercooled liquid state, known as high-density liquid (HDL). We here show that, in line with these earlier reports but without the polyamorphic transition, HGW ends up in a diffusive low-density state (LDL), despite going through a completely different thermal pathway. However, these liquids are prone to crystallization, and to study them in a wider temperature range requires shorter time scales. Several studies deal with crystallization [74] or polyamorphic transformations of HDA [75], LDA [76], and very high-density amorphous ice (VHDA) [77] by rapid laser heating on timescales of nano- to microseconds. In essence, they all find liquid-liquid

transitions between LDL and HDL but using completely different thermal pathways. This, in line with the mentioned XPCS studies, suggests that water's deeply supercooled liquids are distinct metastable phases that are reached in equilibrium, regardless of thermal history.

In summary, we here report that amorphous ice, in our case HGW, exhibits significant diffusive and non-diffusive dynamics between 125 and 156 K before crystallizing under reduced pressure (~10^{-4} mbar). The non-diffusive, mainly ballistic, coalescence dynamics are not only fast enough but also on sufficiently large length scales so that major morphological changes can occur. This has implications for cryochemical techniques since not only bulk but also surface dynamics have to be considered when using HGW either as a reaction medium [78] or as a sample matrix for cryo-EM [10]. Based on our data, below 145 K, the diffusion of water molecules can be neglected compared to the length scales of typical biological specimen, such as viruses. However, this is not the case on the interface regions where even at 125 K, dynamics are fast enough to cause changes in morphology and possibly also influence biological samples. To avoid these kind of surface dynamics cryo-electron micrographs need to be recorded well below 125 K.

Acknowledgments

This reseach was funded in part by the Austrian Science Fund (FWF) [Grant-DOI 10.55776/PAT2619124 and 10.55776/P36634]. J.G. and C.M.T. acknowledge funding by the Tyrolean Young Researchers Programme of the state of Tyrol. We acknowledge DESY (Hamburg, Germany), a member of the Helmholtz Association HGF, for the provision of experimental facilities. Parts of this research were carried out at PETRA III. Data was collected using the beamline P10 operated by DESY Photon Science. Beamtime was allocated for proposal T-20220749. This research was supported in part by the Maxwell computational resources operated at DESY, Hamburg, Germany. T.E., C.M.T., A.G. and R.P.C.B. acknowledge funding by the Centre for Molecular Water Science (CMWS) within Early Science Projects. C.M.T. acknowledges funding by PIER - Partnership of University Hamburg and DESY within a PIER Seed Project (Grant No. PIF-2024-05), by the Austrian Academy of Sciences (ÖAW), and by the Austrian Science Fund (FWF) within the Disruptive Innovation-Early Career Seed Money Grant. Funding from the Deutsche Forschungsgemeinschaft (DFG, German Research Foundation) is acknowledged: K.A-W. is member of the GRK 2516 (Grant No. 405552959). I.Z. is the recipient of a doctoral position within the GRK 2516 program. T.E., N.C.G., L.E.K. and K. A.-W. acknowledges funding by DFG in the framework to the collaborative research center "Defects and Defect Engineering in Soft Matter" (SFB1552) under Project No. 465145163 / Q3.

Competing Interest Declaration

The authors declare no conflicts of interest.

Supplementary Material

The supplementary material contains additional information on the samples, details on the temperature calibration procedure and supplementary wide-angle X-ray scattering (WAXS), small-angle X-ray scattering (SAXS) and X-ray photon correlation spectroscopy (XPCS) data.

Author Contributions

Johannes Giebelmann: Data curation (equal); Formal analysis (equal); Investigation (equal); Methodology (equal); Visualization (equal); Writing – original draft (equal); Writing – review & editing (equal). **Tobias Eklund**: Data curation (equal); Formal analysis (equal); Software (equal); Writing – review & editing (equal). **Christina M. Tonauer**: Data curation (equal); Investigation (supporting); Resources (equal). **Lilli-Ruth Fidler**: Data curation (equal); Investigation (supporting). **Louisa E. Kraft**: Data curation (equal); Investigation (supporting). **Isabell Zick**: Data curation (equal); Investigation (supporting). **Niels C. Gießelmann**: Data curation (equal); Investigation (supporting). **Fiona Berner**: Data curation (equal); Investigation (supporting). **Leah Schwerdtfeger:** Data curation (equal); Investigation (supporting). **Randeer Gautam**: Data curation (equal); Investigation

(supporting). **Robert P. C. Bauer**: Data curation (equal); Investigation (supporting). **Alexander Gierke**: Data curation (equal); Investigation (supporting). **Fabian Westermeier**: Formal analysis (equal); Methodology (equal); Resources (equal); Software (equal); Writing – review & editing (supporting). **Felix Lehmkühler**: Formal analysis (equal); Funding acquisition (equal); Investigation (equal); Methodology (equal); Project administration (equal); Resources (equal); Supervision (equal). **Katrin Amann-Winkel**: Conceptualization (equal); Data curation (equal); Funding acquisition (equal); Investigation (equal); Methodology (equal); Project administration (equal); Resources (equal); Supervision (equal); Writing – original draft (equal); Writing – review & editing (equal). **Thomas Loerting**: Conceptualization (equal); Data curation (equal); Funding acquisition (equal); Investigation (equal); Methodology (equal); Project administration (equal); Resources (equal); Supervision (equal); Writing – original draft (equal); Writing – review & editing (equal).

Data Availability

Raw data were generated at the Deutsches Elektronen-Synchrotron DESY (Hamburg, Germany) PETRA III large scale facility within proposal T-20220749. Derived data supporting the findings of this study are available from the corresponding author upon reasonable request.

References

1. C. A. Angell, Annu. Rev. Phys. Chem. **55**, 559 (2004).
2. K. I. Öberg, Chem. Rev. **116**, 9631 (2016).
3. N. Giovambattista, K. Amann-Winkel, and T. Loerting in *Liquid polymorphism*, edited by H. E. Stanley (Wiley, Hoboken, NJ, 2013), Vol. 152, p. 139.
4. J. A. Searles, J. F. Carpenter, and T. W. Randolph, Food Biophys. **90**, 872 (2001).
5. G. Petzold and J. M. Aguilera, Food Biophys. **4**, 378 (2009).
6. T. Chang and G. Zhao, Adv. Sci. **8**, 2002425 (2021).
7. R. A. Steinbrecht and K. Zierold, *Cryotechniques in Biological Electron Microscopy* (Springer Berlin Heidelberg, Berlin, Heidelberg, 1987).
8. E. Mayer, J. Appl. Phys. **58**, 663 (1985).
9. J. Dubochet, M. Adrian, J.-J. Chang, J. Lepault, and A. W. McDowall in *Cryotechniques in Biological Electron Microscopy*, edited by R. A. Steinbrecht and K. Zierold (Springer Berlin Heidelberg, Berlin, Heidelberg, 1987), p. 114.
10. L. Bachmann and E. Mayer in *Cryotechniques in Biological Electron Microscopy*, edited by R. A. Steinbrecht and K. Zierold (Springer Berlin Heidelberg, Berlin, Heidelberg, 1987), p. 3.
11. G. Weissenberger, R. J. M. Henderikx, and P. J. Peters, Nat. Methods **18**, 463 (2021).
12. U. H. Ermel, H. Schwalbe, and A. V. Cherepanov, Chem. Eur. J. **31**, e202403878 (2025).
13. I. Kohl, L. Bachmann, A. Hallbrucker, E. Mayer, and T. Loerting, Phys. Chem. Chem. Phys. **7**, 3210 (2005).
14. N. J. Mowry, C. R. Krüger, M. Drabbels, and U. J. Lorenz, Phys. Rev. Res. **7** (2025).
15. J. M. Voss, O. F. Harder, P. K. Olshin, M. Drabbels, and U. J. Lorenz, Struct. dyn. **8**, 54302 (2021).
16. J. M. Voss, O. F. Harder, P. K. Olshin, M. Drabbels, and U. J. Lorenz, Chem. Phys. Lett. **778**, 138812 (2021).
17. A. V. Cherepanov and H. Schwalbe, Chem. Methods **3**, e202200050 (2023).
18. J. Giebelmann, T. Eklund, U. Boesenberg, J.-E. Pudell, W. Jo, J. Möller, A. Rodriguez-Fernandez, J. Wrigley, A. Zozulya, A. Madsen, P. Bartl, F. Berner, R. Bauer, N. Giesselmann, A. Gierke, R. Štůsek, L. Veselý, D. Heger, C. Goy, G. Grübel, F. Lehmkuhler, K. Amann-Winkel, and T. Loerting, Under Review, DOI: 10.21203/rs.3.rs-5112004/v2 (2025).
19. Y. P. Handa and D. D. Klug, J. Phys. Chem. **92**, 3323 (1988).
20. M. S. Elsaesser, K. Winkel, E. Mayer, and T. Loerting, Phys. Chem. Chem. Phys. **12**, 708 (2010).
21. R. S. Smith and B. D. Kay, Nature **398**, 788 (1999).

22. G. A. Kimmel, M. K. Dunlap, K. Gurdumov, R. S. Smith, L. Kringle, and B. D. Kay, J. Chem. Phys. **162**, 244505 (2025).
23. F. Perakis, K. Amann-Winkel, F. Lehmkühler, M. Sprung, D. Mariedahl, J. A. Sellberg, H. Pathak, A. Späh, F. Cavalca, D. Schlesinger, A. Ricci, A. Jain, B. Massani, F. Aubree, C. J. Benmore, T. Loerting, G. Grübel, L. G. M. Pettersson, and A. Nilsson, Proc. Natl. Acad. Sci. USA **114**, 8193 (2017).
24. T. Eklund, C. M. Tonauer, K. Yamashita, J. Giebelmann, L.-R. Fidler, A. Karina, H. Li, L. Kraft, F. Berner, N. C. Gießelmann, R. Bauer, A. Gierke, C. Goy, M. Ladd-Parada, F. Perakis, F. Westermeier, F. Lehmkühler, T. Loerting, and K. Amann-Winkel, J. Chem. Phys. **164**, 14501 (2026).
25. K. Amann-Winkel, C. Gainaru, P. H. Handle, M. Seidl, H. Nelson, R. Böhmer, and T. Loerting, Proc. Natl. Acad. Sci. USA **110**, 17720 (2013).
26. G. P. Johari, Phys. Chem. Chem. Phys. **7**, 1091 (2005).
27. G. P. Johari, J. Chem. Phys. **122**, 144508 (2005).
28. G. P. Johari, J. Phys. Chem. B **102**, 4711 (1998).
29. M. Fisher and J. P. Devlin, J. Phys. Chem. **99**, 11584 (1995).
30. J. J. Shephard, J. S. O. Evans, and C. G. Salzmann, J. Phys. Chem. Lett. **4**, 3672 (2013).
31. J. J. Shephard and C. G. Salzmann, J. Phys. Chem. Lett. **7**, 2281 (2016).
32. J. H. Melillo, D. Cangialosi, V. Di Lisio, E. Steinrücken, M. Vogel, and S. Cerveny, Proc. Natl. Acad. Sci. USA **121**, e2407030121 (2024).
33. Y. Yue and C. A. Angell, Nature **435**, E1-E2 (2005).
34. K. Amann-Winkel, R. Böhmer, F. Fujara, C. Gainaru, B. Geil, and T. Loerting, Rev. Mod. Phys. **88**, 11002 (2016).
35. G. Grübel and F. Zontone, J. Alloys Compd. **362**, 3 (2004).
36. F. Lehmkühler, W. Roseker, and G. Grübel, Appl. Sci. **11**, 6179 (2021).
37. A. R. Sandy, Q. Zhang, and L. B. Lurio, Annu. Rev. Mater. Res. **48**, 167 (2018).
38. A. Madsen, A. Fluerasu, and B. Ruta in *Synchrotron Light Sources and Free-Electron Lasers. Accelerator Physics, Instrumentation and Science Applications*, edited by E. J. Jaeschke, S. Khan, J. R. Schneider, and J. B. Hastings (Springer, Cham, Switzerland, 2020), p. 1989.
39. M. Sikorski, Z. Jiang, M. Sprung, S. Narayanan, A. R. Sandy, and B. Tieman, Nucl. Instrum. Methods Phys. Res. A. **649**, 234 (2011).
40. A. Duri and L. Cipelletti, Europhys. Lett. **76**, 972 (2006).
41. J. Kieffer and D. Karkoulis, J. Phys.: Conf. Ser. **425**, 202012 (2013).
42. L. A. Feign and D. I. Svergun, *Structure Analysis by Small-Angle X-Ray and Neutron Scattering* (Springer US, Boston, MA, 1987).
43. A. Madsen, R. L. Leheny, H. Guo, M. Sprung, and O. Czakkel, New J. Phys. **12**, 55001 (2010).
44. Y. Yue, J. Non-Cryst. Solids: X **14**, 100099 (2022).
45. P. H. Handle, L. Rovigatti, and F. Sciortino, Phys. Rev. Lett. **122**, 175501 (2019).
46. G. Nava, M. Rossi, S. Biffi, F. Sciortino, and T. Bellini, Phys. Rev. Lett. **119**, 78002 (2017).
47. N. Nemoto, A. Koike, and K. Osaki, Macromolecules **29**, 1445 (1996).
48. L. Rovigatti, G. Nava, T. Bellini, and F. Sciortino, Macromolecules **51**, 1232 (2018).
49. H. Li, M. Ladd-Parada, A. Karina, F. Dallari, M. Reiser, F. Perakis, N. N. Striker, M. Sprung, F. Westermeier, G. Grübel, W. Steffen, F. Lehmkühler, and K. Amann-Winkel, J. Phys. Chem. Lett. **14**, 10999 (2023).
50. A. Karina, H. Li, T. Eklund, M. Ladd-Parada, B. Massani, M. Filianina, N. Kondedan, A. Rydh, K. Holl, R. Trevorah, S. Huotari, R. P. C. Bauer, C. Goy, N. N. Striker, F. Dallari, F. Westermeier, M. Sprung, F. Lehmkühler, and K. Amann-Winkel, Commun. Chem. **8**, 82 (2025).
51. M. Ladd-Parada, H. Li, A. Karina, K. H. Kim, F. Perakis, M. Reiser, F. Dallari, N. Striker, M. Sprung, F. Westermeier, G. Grübel, A. Nilsson, F. Lehmkühler, and K. Amann-Winkel, Environmental science: atmospheres **2**, 1314 (2022).
52. A. J. Mueller, A. P. Lindsay, R. M. Lewis, Q. Zhang, S. Narayanan, T. P. Lodge, M. K. Mahanthappa, and F. S. Bates, Physical review letters **132**, 158101 (2024).

53. E. Thoms, J. P. Gabriel, and R. Richert, Phys. Rev. Lett. **135**, 28001 (2025).
54. T. Eklund, C. M. Tonauer, F. Lehmkühler, and K. Amann-Winkel, Photon Sci., accepted for publication 10.1021/photonsci.5c00014 (2025).
55. H. Pollard, Bull. Amer. Math. Soc. **52**, 908 (1946).
56. E. W. Hansen, X. Gong, and Q. Chen, Macro Chemistry & Physics **214**, 844 (2013).
57. S. W. Provencher and P. Štêpánek, Part & Part Syst Charact **13**, 291 (1996).
58. R. Angelini, L. Zulian, A. Fluerasu, A. Madsen, G. Ruocco, and B. Ruzicka, Soft Matter **9**, 10955 (2013).
59. C. R. Hill, C. Mitterdorfer, T. G. A. Youngs, D. T. Bowron, H. J. Fraser, and T. Loerting, Phys. Rev. Lett. **116**, 215501 (2016).
60. G. P. Johari, A. Hallbrucker, and E. Mayer, Nature **330**, 552 (1987).
61. J. A. McMillan and S. C. Los, Nature **206**, 806 (1965).
62. I. Kohl, L. Bachmann, E. Mayer, A. Hallbrucker, and T. Loerting, Nature **435**, E1 (2005).
63. M. Seidl, M. S. Elsaesser, K. Winkel, G. Zifferer, E. Mayer, and T. Loerting, Phys. Rev. B **83**, 100201(R) (2011).
64. K. L. Ngai, Y. Zhang, S. Capaccioli, and L.-M. Wang, J. Chem. Phys. **164** (2026).
65. D. T. Bowron, J. L. Finney, A. Hallbrucker, I. Kohl, T. Loerting, E. Mayer, and A. K. Soper, J. Chem. Phys. **125**, 194502 (2006).
66. Y. Yue and C. A. Angell, Nature **427**, 717 (2004).
67. C. Austen Angell, Science (2008).
68. G. P. Johari, J. Chem. Phys. **117**, 2782 (2002).
69. V. Fuentes-Landete, L. J. Plaga, M. Keppler, R. Böhmer, and T. Loerting, Phys. Rev. X **9** (2019).
70. T. Reinot, N. C. Dang, and R. Jankowiak, J. Phys. Chem. B **113**, 4303 (2009).
71. H. Schober, M. M. Koza, A. Tölle, C. Masciovecchio, F. Sette, and F. Fujara, Phys. Rev. Lett. **85**, 4100 (2000).
72. M. M. Koza, H. Schober, B. Geil, M. Lorenzen, and H. Requardt, Phys. Rev. B **69**, 24204 (2004).
73. K. L. Ngai, Y. Zhang, S. Capaccioli, and L.-M. Wang, Chem. Phys. **596**, 112748 (2025).
74. M. Ladd-Parada, K. Amann-Winkel, K. H. Kim, A. Späh, F. Perakis, H. Pathak, C. Yang, D. Mariedahl, T. Eklund, T. J. Lane, S. You, S. Jeong, M. Weston, J. H. Lee, I. Eom, M. Kim, J. Park, S. H. Chun, and A. Nilsson, J. Phys. Chem. B **126**, 2299 (2022).
75. K. H. Kim, K. Amann-Winkel, N. Giovambattista, A. Späh, F. Perakis, H. Pathak, M. L. Parada, C. Yang, D. Mariedahl, T. Eklund, T. J. Lane, S. You, S. Jeong, M. Weston, J. H. Lee, I. Eom, M. Kim, J. Park, S. H. Chun, P. H. Poole, and A. Nilsson, Science **370**, 978 (2020).
76. K. Amann-Winkel, K. H. Kim, N. Giovambattista, M. Ladd-Parada, A. Späh, F. Perakis, H. Pathak, C. Yang, T. Eklund, T. J. Lane, S. You, S. Jeong, J. H. Lee, I. Eom, M. Kim, J. Park, S. H. Chun, P. H. Poole, and A. Nilsson, Nat. Commun. **14**, 442 (2023).
77. C. Yang, M. Ladd-Parada, K. Nam, S. Jeong, S. You, T. Eklund, A. Späh, H. Pathak, J. H. Lee, I. Eom, M. Kim, F. Perakis, A. Nilsson, K. H. Kim, and K. Amann-Winkel, J. Chem. Phys. **160** (2024).
78. K. Winkel, W. Hage, T. Loerting, S. L. Price, and E. Mayer, J. Am. Chem. Soc. **129**, 13863 (2007).